EUROPEAN JOURNAL OF PURE AND APPLIED MATHEMATICS
2025, Vol. 18, Issue 4, Article Number 7138
ISSN 1307-5543 – ejpam.com
Published by New York Business Global

Mathematical Analysis for Magnetohydrodynamic Peristaltic Flow of Cerebrospinal Fluid in the Glymphatic System

M. A. El-Shorbagy[1], Ahmed A. Elsawy[2], Abdallah A. Henedy[2,3], Hossam A. Nabwey[1], B. Alreshidi[1], Essam T. Abdelwahab[2,3,*]

[1] *Department of Mathematics, College of Science and Humanities in Al-Kharj, Prince Sattam bin Abdulaziz University, Al-Kharj 11942, Saudi Arabia*
[2] *Basic Engineering Sciences Department, Faculty of Engineering, Menoufia University, Shebin El-Kom, Egypt*
[3] *Faculty of Engineering, Menoufia National University, Menoufia, Shebin El-Kom, Egypt*

Abstract. Cerebrospinal fluid (CSF) flow within perivascular routes (PVS) is essential for maintaining brain health and function. This flow is a part of the glymphatic system, which clears waste products and metabolic byproducts from the brain. The PVS boundaries consist of a non-permeable arterial vessel wall and neural tissue. The arterial vessel peristalsis and the elasticity of the neural tissue are responsible for generating the CSF flow. This article examines the effect of a transverse magnetostatic field and pertinent physiological conditions on CSF flow. It specifically considers the impact of brain elasticity and porosity at the neuroglial layers, arterial wall curvature, and the peristalsis amplitude. The effective Navier–Stokes governing equations describe the peristalsis of CSF flow subjected to a magnetostatic field. The perturbation strategy is utilized to address the governing equations. This leads to a set of equations describing CSF stream-direction velocity, pressure gradient, and neural tissue deformation. The graphical outcomes highlight the significant influence of a range of physiological and flow factors on the behavior of CSF. The key parameters encompass neural tissue porosity and stiffness, neuroglial layer deformation, magnetostatic field strength, and arterial wall curvature. The results reveal that enhancing the magnetostatic field intensity reduces CSF pressure distribution, stream-direction velocity, and arterial deformation. The numerical computations and graphical representations of the obtained analytical solutions are performed using the MATLAB software package. This study is highly significant due to its implications for the development and advancement of different neurological disorders for instance Alzheimer's disease, meningeal inflammation, neurotrauma, and hemorrhagic stroke.

2020 Mathematics Subject Classifications: 76W05, 76Z05, 92C35, 74F10

Key Words and Phrases: Perturbation method, peristalsis, magnetostatic field, glymphatic network, CSF

*Corresponding author.
DOI: https://doi.org/10.29020/nybg.ejpam.v18i4.7138

Email addresses: essam.tharwat@sh-eng.menofia.edu.eg (E. T. Abdelwahab)

Nomenclature

r	The radial coordinate axis
z	The stream-direction axis
b	The PVS thickness
r_1	The arterial vessel average radius
r_2	The neural tissue lumen radius
$h(z,t)$	The wall deformation
$\bar{h}$	The peristalsis amplitude
λ	The peristalsis wavelength
t	Time frame
d	The deformation of neuroglial layer
c	The peristalsis speed
p	The CSF pressure
D	The neuroglial elastic layer deformation with neural tissue
P_e	The neural tissue pressure
P_a, P_b	The Pressure values at the extreme points of the PVS ($P_a > P_b$)
P_o	The zeroth-order pressure
M_e	The neural tissue porosity
E_e	The neural tissue stiffness
E_a	The arterial vessel wall elastic modulus
E_g	The neural tissue Young's modulus
K_g	The neuroglial layer porosity parameter
t_a	The arterial vessel layer thickness
R_e	Reynolds number
μ	The CSF dynamic viscosity
ρ	The CSF density
ε	PVS film thickness
B	Hartmann number
σ	Electrical conductivity
β_o	Magnetic field strength
W_o	The zeroth order stream-direction flow velocity
U_o	The zeroth order radial flow velocity
U_e	The permeation velocity
$\vec{n}$	The elastic neuroglial layer normal unit vector
$\vec{t}$	The elastic neuroglial layer tangent unit vector
$\vec{V}$	The vector of velocity field
$\hat{e_r}$	The radial unit vector
$\hat{e_z}$	The stream-direction unit vector
U	The radially oriented velocity
W	The stream-direction velocity
R_1	The PVS layer lumen radius
R_2	The PVS layer exoradius
ω	The peristalsis frequency in the arterial vessel
L	The PVS length

1. Introduction

The glymphatic system is an indispensable brain-wide PVS network responsible for removing metabolic waste products and regulating water balance in the brain. This mechanism function involves driving CSF function along the periarterial spaces and supporting the astrocyte-mediated fluid interchange between the interstitial fluid (ISF) and CSF. This intricate mechanism is essential for preserving brain activity and function especially during sleep and anesthesia [1]. Disruptions in its function is associated to a range of pathological and neurological conditions, including aging, Alzheimer's disease, hemorrhagic stroke, and neurotrauma [2, 3]. The dynamics of CSF are regulated by various elements including arterial pulsation, respiration, posture, and sleep quality. This highlights the strong influence of maintaining normal sleep patterns on glymphatic function and overall brain activity [4, 5].

CSF is a vital, clear, and colorless liquid that envelops the central nervous system (CNS) and serves an essential role in providing nourishment, safeguarding the brain, and removing waste products from this essential organ [6]. This vital fluid also maintains brain stability by controlling chemical composition and temperature. Additionally, it serves a crucial function by protecting the brain from mechanical trauma and supporting fragile nervous tissue [7]. The dynamics of peristalsis exist due to the alternating contraction and expansion of the flexible walls of a distensible channel fluid. It occurs in hollow organs such as the esophagus, stomach, intestines, urine motion in the ureter, chyme movement through the gastrointestinal system, blood transport through cardiovascular network, as well as CSF in the glymphatic system. Several recent theoretical studies investigated the peristaltic transport of biofluids within different conduits and their interaction with various physiological and flow factors [8–20]. Peristaltic motion plays a crucial role in the glymphatic system, facilitating the transport of CSF within the brain. In the context of the glymphatic system, peristalsis in combination with other mechanisms such as longitudinal pressure gradients and directional flow resistance contributes to driving fluid flow through the para-arterial spaces surrounding cerebral arteries [21–24]. The intricate and synchronized movement of neuroglial and arterial walls plays a pivotal role in enabling the glymphatic system to perform essential functions such as effectively clearing waste, facilitating the movement of ISF, and potentially contributing to the maintenance of brain immunity [25].

The influence of magnetostatic fields on CSF flow is a nuanced topic that bridges the disciplines of medical imaging, neurobiology, and biophysics with significant implications for both diagnostic and therapeutic practices. Magnetostatic resonance imaging (MRI), an essential method of modern neuroimaging, leverages strong magnetostatic fields to produce high-resolution images of the brain and spinal cord and is capable of visualizing CSF dynamics using techniques such as phase-contrast MRI. These imaging modalities are instrumental in diagnosing and monitoring conditions like hydrocephalus, where CSF flow is disrupted [26]. Theoretical frameworks such as magnetohydrodynamics (MHD) postulate that magnetostatic fields can influence the behavior of conductive fluids. While CSF is predominantly composed of water and exhibits low ionic conductivity, the presence

of ions and charged particles suggests that strong magnetostatic fields, such as those used in high-field MRI scanners, could potentially induce subtle alterations in CSF flow dynamics. Understanding these potential interactions is vital for optimizing MRI protocols and improving the accuracy of CSF flow measurements [27].

Therapeutic applications of magnetostatic fields are gaining attention for their potential to influence CSF flow and mitigate hemorrhagic stroke-related complications. One of the most promising techniques is magnetostatic resonance-guided focused ultrasound. This noninvasive treatment leverages magnetostatic fields to guide focused ultrasound waves, creating precise openings in neural tissue to enhance CSF drainage. It is particularly beneficial in treating hydrocephalus, a condition often seen in hemorrhagic stroke patients where CSF accumulates due to impaired drainage pathways. By facilitating better CSF flow, magnetostatic resonance-guided focused ultrasound can reduce intracranial pressure and alleviate symptoms associated with fluid buildup.

Additionally, electromagnetic fields are being explored for their neuromodulator effects, which could indirectly benefit CSF dynamics. The modulation of electromagnetic fields might also help in normalizing disrupted CSF flow patterns caused by hemorrhagic stroke-induced brain damage and swelling [28]. Moreover, advances in technology have led to the development of devices that use electromagnetic fields to regulate intracranial pressure. These devices aim to stabilize CSF flow and reduce the complications arising from abnormal CSF dynamics, providing a noninvasive therapeutic option for hemorrhagic stroke patients. In summary, therapeutic methods utilizing magnetostatic fields, such as magnetostatic resonance-guided focused ultrasound and electromagnetic neuromodulation, offer promising avenues for managing CSF flow abnormalities in hemorrhagic stroke patients. These techniques not only enhance CSF drainage and reduce intracranial pressure but also hold potential for broader applications in improving brain function and promoting recovery after hemorrhagic stroke. The nonionizing constant magnetostatic fields produced by devices like smartphones and headphones, as well as mobile network towers, can have varying effects on the CSF in humans, including children. Lonappan et al. [29] demonstrated that exposure to these electromagnetic fields can induce distinct changes in the dielectric parameters of CSF, with both normal and abnormal samples exhibiting different behaviors in terms of dielectric constant and conductivity at specific frequencies. Additionally, Ali [30] highlighted concerns about the potential neurological effects associated with the emitted mobile phone electromagnetic radiation, including cognitive dysfunction and neurogenesis impairment. While there is ongoing debate about the safety of exposure to electromagnetic fields, especially from mobile devices, Preece [31] suggested that a short-term exposure within established guidelines may not pose a significant risk to humans.

Moreover, Romanò et al. [22] presented a dominant order approximation of the momentum equations with lubrication approximation for investigating the flow of CSF through the glymphatic system. The effects of a peristaltic wave in the arterial vessel and the deformability of neural tissue were considered as a motive force for the flow. Additionally, they justified the negligible importance of convective transport compared to diffusion effects in the PVS using first principles and dimensional analysis considerations. Sub-

sequently, they focused on computing the leak velocity of CSF between the PVS space and brain interstation using their first-principles approach. Furthermore, Preece [31] concentrated on the fluid dynamics of CSF along the PVS in the spinal cord. A detailed numerical analysis was conducted based on the lubrication approximation, utilizing criteria such as long wavelength and low Reynolds number. They indicated the strong effect of interaction between the peristalsis induced by the arterial vessel wall and the flow associated with a convection-enhanced delivery infusion, especially at distances far from the infusion source. The model undertaken examined the axial transport in a circular area with non-permeable boundaries, but it did not investigate fluid transport across the tissue layer. On the other hand, Schley et al. [32] formulated a mathematical framework to examine the hypothesis that the PVS drainage of ISFs and solutes out of neural tissue is driven by pulsations of arterial walls. Prior empirical studies [33–35] demonstrated that the CSF transport is substantially influenced by the elastic features of blood vessel walls, the wall porosity of neural tissue, and the pulsation of the blood flow. However, the inherent difficulty of measuring these parameters in vivo necessitates the use of modeling-based approaches to enhance our understanding of fluid transport within the brain. To preserve neuro homeostasis, the glymphatic system promotes the dynamics of CSF for metabolic waste products to be removed from neural tissue. This mechanism is related to the onset of various neurological disorders involving traumatic brain injury, Parkinson's, and Alzheimer's diseases. Therefore, knowledge of the dynamics of CSF flow within the glymphatic network is necessary to identify the mechanisms underlying these conditions. Recent studies [36–43] indicate that magnetic fields can alter the movement of charged particles and ionic species in biological fluids, thereby altering transport phenomena at the microvascular and perivascular scales. Magnetic fields have a potential impact on the flow of ionic species and charged particles contained in biofluids through microvascular and perivascular mechanisms. Magnetostatic fields can affect flow resistance and enhance solute transport performance. The interaction between the induced electric currents and magnetic fields produces the Lorentz force. This force can alter CSF flow rates, pressure gradients, and velocity profiles. A helpful framework for investigating possible alterations to glymphatic transport pathways brought on by internal or external magnetic fields is provided using MHD models.

The primary motivation of this study is to develop a mathematical formulation of PVS transport under a magnetostatic field to provide insights into how the factors of brain elasticity and porosity at the neuroglial layer boundaries, the arterial wall curvature, the strength of the magnetostatic field, and the peristalsis amplitude affect the direction and quantity of CSF flow. To achieve a dominant-order features of CSF flow, this model will neglect the influence of ciliated boundaries and non-Newtonian behavior [44–46]. The PVS is modeled to contain a Newtonian incompressible fluid of constant viscosity. The model described in this paper builds upon previous methods for calculating PVS fluid flow in simplified shapes under the influence of a transverse magnetostatic field. In this model, the Navier–Stokes equations are addressed using lubrication theory approximations following the steps of the semi-analytical perturbation technique. This study displays the promising influences of the magnetostatic field on CSF flow and brain health. This

investigation is essential as it explores the complex mechanisms involved in the peristaltic flow of CSF within the glymphatic system in the presence of a magnetostatic field and its direct relevance to the development of diverse neurological disorders, including Alzheimer's disease, hemorrhagic stroke, and meningeal inflammation.

It should be noticed that this study assumes constant physical properties and a steady-state flow regime. This assumption simplifies the actual physiological conditions of CSF motion within the glymphatic system. CSF flow is driven by pulsatile pressure variations associated with cardiac activity. Its rheological and transport properties can vary due to interactions with the surrounding neural tissues. This simplification results in a steady state approach which provides an essential theoretical framework for the MHD-induced CSF transport. It highlights the strong influence of magnetic, viscous, and porosity effects on PVS dynamics. Future studies could extend the present model to incorporate time dependent pulsatile effects, and temperature dependent variable viscosity of CSF to achieve a more comprehensive physiological representation.

2. Mathematical Modelling

2.1. Structural Geometry

The model structure of the PVS space that transports the CSF is characterized as a thin annulus space surrounded by the walls of a non-permeable elastic arterial vessel and neural tissues (Figure 1). The neural tissue is padded from the inside by a porous, elastic neuroglial wall, which separates the PVS from the neural tissue [22]. This neuroglial wall is modeled with the tube law. The elastic tube law describes how the elastic properties of pulsating walls in physiological systems can be modeled. Experimentally, it is simulated by finite length rubber tubes that demonstrate a diverse self-sustained oscillation, providing insight into the underlying dynamics system. It is used to define the interaction between the peristaltic deformation of the solid walls and the pressure difference of the CSF across them. The blood pulsation in the arterial vessel generates consequential sinusoidal waves, which represent the peristaltic deformation. This model is exposed to an external transverse magnetostatic field. It is applicable in cases of diagnostic and therapeutic applications, such as MRI for visualizing the CSF dynamics in the brain and magnetostatic resonance-guided focused ultrasound as a therapeutic method for brain hemorrhagic stroke treatment. The ISF is used as a constant reference pressure. The cylindrical frame (R-Z) is chosen to represent the CSF flow in the PVS structure, The peristalsis propagates according to

$$h(z,t) = \bar{h}\sin\left[\frac{2\pi}{\lambda}(z-ct)\right],$$

and the permeable elastic neuroglial wall is deformed according to $d(z,t)$.

The PVS geometry is mapped to the glymphatic system with elastic annular structure to depict the anatomical arrangement where cerebrospinal fluid flows around cerebral arteries. This arrangement is surrounded on the inside by the arterial wall and on the

outside by the permeable astrocytic layer. This model approaches the real PVS system and refers to a good agreement with physiological structure that has been incorporated, see Figure 2. In this study, a uniform magnetostatic field of strength β_0 is applied transversely to the direction of peristaltic motion of CSF within the tube. The magnetic field is oriented perpendicular to the streamwise direction (r-direction). This configuration is consistent with the approach used in low magnetic Reynolds number MHD flows in which the induced magnetic field is negligible compared to the applied field. Under these conditions, the Lorentz force $F_L = \sigma\beta_0^2 w$ acts as a resistive body force opposing the motion. The constancy of β_0 emphasizes that magnetic effects remain spatially uniform across the domain. The PVS walls are assumed to be non-conducting, ensuring that the tangential component of the magnetic field remains continuous across the boundaries.

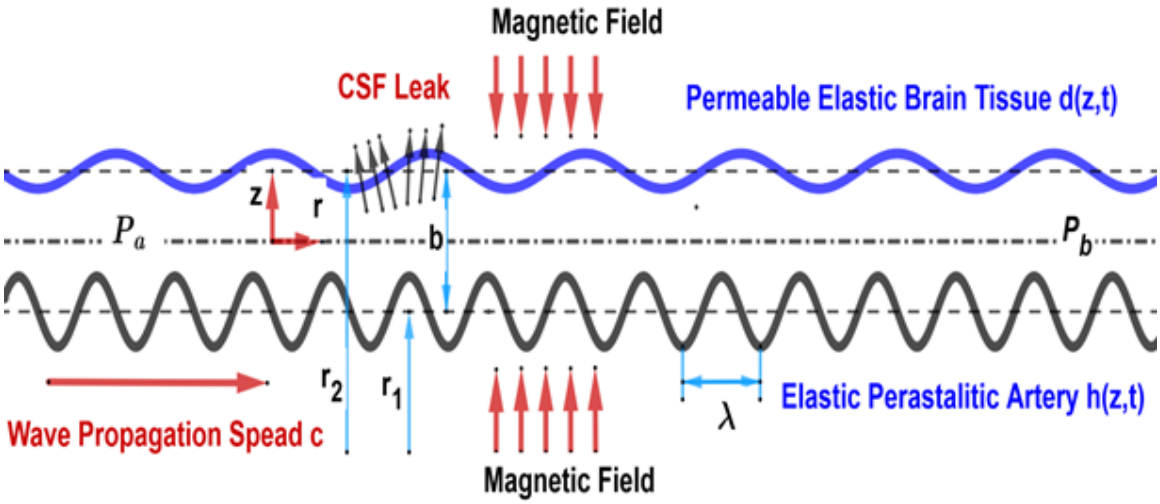

Figure 1: Schematic graph for the PVS space between the elastic neural tissue and the arterial vessel, including the peristalsis and transversal magnetostatic field.

2.2. Mathematical Formulation

The transformation of the cylindrical framework from the unsteady frame (r, z) to the steady one (R, Z) using the same wave speed c requires the following method:

$$R = r, \quad Z = z - ct, \quad U(R, Z, T) = u(r, z, t), \quad W(R, Z, T) = w(r, z, t), \quad P(R, Z, T) = p(r, z, t).$$

The Navier–Stokes equations for the CSF flow with constant viscosity across the elastic PVS structure are represented as follows [22, 47]:

Governing Equations:

Continuity

$$\frac{1}{r}\frac{\partial(ru)}{\partial r} + \frac{\partial w}{\partial z} = 0 \tag{1}$$

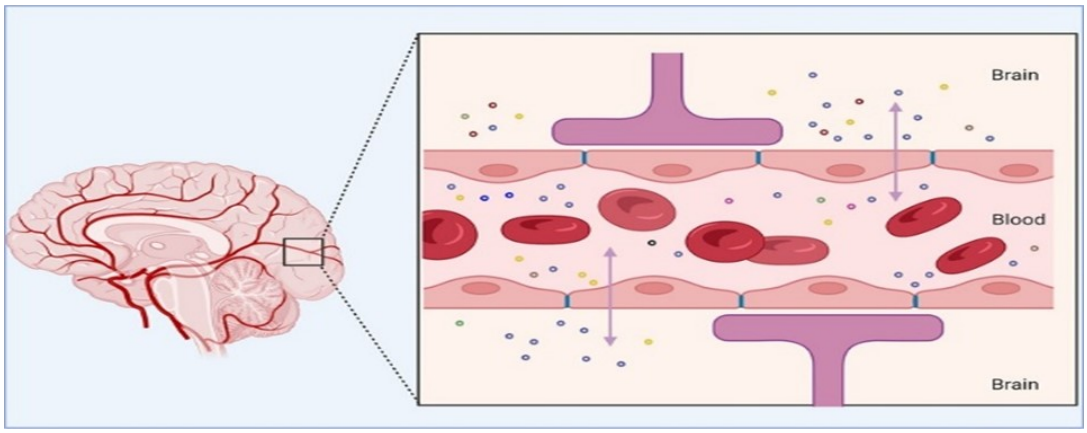

Figure 2: Real physiological structure of PVS system.

r-momentum

$$\frac{\partial u}{\partial t}+u\frac{\partial u}{\partial r}+w\frac{\partial u}{\partial z}=-\frac{1}{\rho}\frac{\partial p}{\partial r}+\frac{\mu}{\rho}\left[\frac{1}{r}\frac{\partial u}{\partial r}+\frac{\partial^2 u}{\partial r^2}+\frac{\partial^2 u}{\partial z^2}\right] \tag{2}$$

z-momentum

$$\frac{\partial w}{\partial t}+u\frac{\partial w}{\partial r}+w\frac{\partial w}{\partial z}=-\frac{1}{\rho}\frac{\partial p}{\partial z}+\frac{\mu}{\rho}\left[\frac{1}{r}\frac{\partial w}{\partial r}+\frac{\partial^2 w}{\partial r^2}+\frac{\partial^2 w}{\partial z^2}\right]-\sigma\beta_0^2 w \tag{3}$$

Peristaltic propagation of the arterial vessel wall about the mean radii

$$h(z,t)=\bar{h}\sin\left[\frac{2\pi}{\lambda}(z-ct)\right] \tag{4}$$

Boundary conditions:
Nonslip case at the elastic arterial vessel $r=r_1+h$

$$w(r,z,t)=0 \tag{5}$$

$$u(r,z,t)=\frac{\partial h(z,t)}{\partial t} \tag{6}$$

Porosity case at the elastic neuroglial layer $r=r_1+b+d_0$

$$\vec{u}\cdot\vec{n}=\frac{\partial d}{\partial t}+M_e(p-p_e) \tag{7}$$

$$\vec{u}\cdot\vec{t}=0 \tag{8}$$

$$d=\frac{p-p_e}{E_e} \tag{9}$$

CSF pressure at the PVS inlet $z=0$ **and outlet** $z=l$

$$p=p_a \text{ at } z=0 \tag{10}$$

$$p = p_b \text{ at } z = l \tag{11}$$

Dimensionless parameters:

$$\begin{aligned} &r = bR, \qquad z = \lambda Z, \qquad t = T/\omega, \qquad u = b\omega U, \quad w = \lambda\omega W, \\ &p = \frac{\mu\omega}{\epsilon^2}P, \quad B^2 = \frac{\sigma\beta_0^2 b^2}{\mu}, \quad p_a = \frac{\mu\omega}{\epsilon^2}P_a, \quad p_b = \frac{\mu\omega}{\epsilon^2}P_b \end{aligned} \tag{12}$$

$$\begin{aligned} &\omega = \frac{c}{\lambda}, \qquad \epsilon = \frac{b}{\lambda}, \qquad Re = \frac{\epsilon\rho\omega b^2}{\mu}, \quad H = \frac{h}{b}, \\ &R_1 = \frac{r_1}{b}, \quad R_2 = \frac{r_2}{b} = R_1 + 1, \quad D_0 = \frac{d}{b}, \qquad l = \lambda L \end{aligned} \tag{13}$$

Applying the nondimensional parameters (12-13) to the governing equations (1-4) and their boundary conditions (5-11) yields the following nondimensional sets of equations.

Dimensionless governing equations:

$$\frac{1}{R}\frac{\partial(RU)}{\partial R} + \frac{\partial W}{\partial Z} = 0 \tag{14}$$

$$\epsilon Re\left[\frac{\partial U}{\partial T} + U\frac{\partial U}{\partial R} + W\frac{\partial U}{\partial Z}\right] = -\frac{\partial P}{\partial R} + \epsilon^2\left[\frac{1}{R}\frac{\partial U}{\partial R} + \frac{\partial^2 U}{\partial R^2} + \frac{b^2}{\lambda^2}\frac{\partial^2 U}{\partial Z^2}\right] \tag{15}$$

$$\epsilon Re\left[\frac{\partial W}{\partial T} + U\frac{\partial W}{\partial R} + W\frac{\partial W}{\partial Z}\right] = -\frac{\partial P}{\partial Z} + \left[\frac{1}{R}\frac{\partial W}{\partial R} + \frac{\partial^2 W}{\partial R^2} + \epsilon^2\frac{\partial^2 W}{\partial Z^2}\right] - \frac{\epsilon^2\lambda^2\rho\sigma\beta}{\mu}W \tag{16}$$

Dimensionless peristaltic deformation of the arterial vessel:

$$H = \bar{H}\sin[2\pi(Z - T)] \tag{17}$$

Nonslip wall conditions at $R = R_1 + H$:

$$W(R, Z, T) = 0 \tag{18}$$

$$U(R, Z, T) = \frac{\partial H(Z, T)}{\partial T} \tag{19}$$

Permeable wall conditions $R_2 = R_1 + 1 + D$:

$$\vec{V}\cdot\vec{n} = \frac{\partial D}{\partial T} + M_e(P - P_e) \Rightarrow U = \frac{\partial D}{\partial T} + M_e(P - P_e) \tag{20}$$

$$\vec{V}\cdot\vec{t} = 0 \Rightarrow W = 0 \tag{21}$$

$$\vec{V} = U\hat{e}_r + W\hat{e}_z, \quad \vec{n} = 1\hat{e}_r + 0\hat{e}_z, \quad \vec{t} = 0\hat{e}_r + 1\hat{e}_z \tag{22}$$

$$D = \frac{P - P_e}{E_e} \tag{23}$$

The pressure conditions at the extreme points of the PVS (inlet $Z = 0$ and outlet $Z = L$):

$$P = P_a \text{ at } Z = 0 \tag{24}$$
$$P = P_b \text{ at } Z = L \tag{25}$$

Method of Solution: The semi-analytical perturbation strategy expands the flow quantities as a power series with a small wave number ϵ as follows:

$$W = W_0 + \epsilon W_1 + \epsilon^2 W_2 + \epsilon^3 W_3 + \cdots \tag{26}$$
$$U = U_0 + \epsilon U_1 + \epsilon^2 U_2 + \epsilon^3 U_3 + \cdots \tag{27}$$
$$P = P_0 + \epsilon P_1 + \epsilon^2 P_2 + \epsilon^3 P_3 + \cdots \tag{28}$$
$$D = D_0 + \epsilon D_1 + \epsilon^2 D_2 + \epsilon^3 D_3 + \cdots \tag{29}$$

Applying the perturbation expansions (26-29) to the governing equations (14-16) with the corresponding boundary conditions (18-25) yields the following sets of differential equations:

The zeroth order set:

$$\frac{1}{R}\frac{\partial (RU_0)}{\partial R} + \frac{\partial W_0}{\partial Z} = 0 \tag{30}$$

$$-\frac{\partial P_0}{\partial R} = 0 \tag{31}$$

$$-\frac{\partial P_0}{\partial Z} + \frac{1}{R}\frac{\partial W_0}{\partial R} + \frac{\partial^2 W_0}{\partial R^2} - \frac{b^2 \rho \sigma \beta^2}{\mu} W_0 = 0 \tag{32}$$

Nonslip case $R = R_1 + H$:

$$W_0(R, Z, T) = 0 \tag{33}$$

$$U_0(R, Z, T) = \frac{\partial H(Z, T)}{\partial T} \tag{34}$$

Permeable case $R_2 = R_1 + 1 + D_0$:

$$W_0 = 0 \tag{35}$$

$$U_0 = \frac{\partial D_0}{\partial T} + M_e(P_0 - P_e) \tag{36}$$

The first order set:

$$\frac{1}{R}\frac{\partial (RU_1)}{\partial R} + \frac{\partial W_1}{\partial Z} = 0 \tag{37}$$

$$-\frac{\partial P_1}{\partial R} = 0 \tag{38}$$

$$R_e\left[\frac{\partial W_0}{\partial T}+U_0\frac{\partial W_0}{\partial R}+W_0\frac{\partial W_0}{\partial Z}\right]=-\frac{\partial P_1}{\partial Z}+\left[\frac{1}{R}\frac{\partial W_1}{\partial R}+\frac{\partial^2 W_1}{\partial R^2}\right] \tag{39}$$

Nonslip case $R=R_1+H$**:**

$$W_1(R,Z,T)=0 \tag{40}$$

$$U_1(R,Z,T)=0 \tag{41}$$

Permeable case $R_2=R_1+1+D_1$**:**

$$W_1=0 \tag{42}$$

$$U_1=\frac{\partial D_1}{\partial T}+M_eP_1 \tag{43}$$

The second order set:

$$\frac{1}{R}\frac{\partial(RU_2)}{\partial R}+\frac{\partial W_2}{\partial Z}=0 \tag{44}$$

$$R_e\left[\frac{\partial U_0}{\partial T}+U_0\frac{\partial U_0}{\partial R}+W_0\frac{\partial U_0}{\partial Z}\right]=-\frac{\partial P_2}{\partial R}+\left[\frac{1}{R}\frac{\partial U_0}{\partial R}+\frac{\partial^2 U_0}{\partial R^2}\right] \tag{45}$$

$$\begin{aligned}R_e\left[\frac{\partial W_1}{\partial T}+U_0\frac{\partial W_1}{\partial R}+U_1\frac{\partial W_0}{\partial R}+W_0\frac{\partial W_1}{\partial Z}+W_1\frac{\partial W_0}{\partial Z}\right]=\\ -\frac{\partial P_2}{\partial Z}+\left[\frac{1}{R}\frac{\partial W_2}{\partial R}+\frac{\partial^2 W_2}{\partial R^2}+\frac{\partial^2 W_0}{\partial Z^2}\right]\end{aligned} \tag{46}$$

Nonslip case $R=R_1+H$**:**

$$W_2(R,Z,T)=0 \tag{47}$$

$$U_2(R,Z,T)=0 \tag{48}$$

Permeable case $R_2=R_1+1+D_2$**:**

$$W_2=0 \tag{49}$$

$$U_2=\frac{\partial D_2}{\partial T}+M_e(P_2) \tag{50}$$

For simplifications, the zeroth-order solution is adequate and guarantee solution convergence, and the subsequent sets are complicated with little significance to the outcomes.

The CSF velocity and the pressure solutions are expressed as follows:

$$W(r)=C_1I_0(\sqrt{B}r)+C_2K_0(\sqrt{B}r)-\frac{1}{B}\frac{dP_0}{dZ} \tag{51}$$

$$U = \frac{1}{\sqrt{B}}\frac{\partial C_2}{\partial Z}K_1(\sqrt{B}r) - \frac{1}{\sqrt{B}}\frac{\partial C_1}{\partial Z}I_1(\sqrt{B}r) + \frac{R}{2B}\frac{d^2P_0}{dZ^2} + \frac{C_3}{R} \tag{52}$$

$$P_0 = C_4 e^{\sqrt{A_1/A_0}Z} + C_5 e^{-\sqrt{A_1/A_0}Z} - \frac{A_2}{A_1} \tag{53}$$

$$\begin{aligned}\frac{\partial P_0}{\partial Z} = \sqrt{\frac{A_1}{A_0}}\left\{P_a + \frac{A_2}{A_1} - \frac{(P_e + A_2/A_1 - [P_a + A_2/A_1]e^{\sqrt{A_1/A_0}L})}{[e^{-\sqrt{A_1/A_0}L} - e^{\sqrt{A_1/A_0}L}]}\right\}e^{\sqrt{A_1/A_0}Z} \\ -\sqrt{\frac{A_1}{A_0}}\frac{(P_e + A_2/A_1 - [P_a + A_2/A_1]e^{\sqrt{A_1/A_0}L})}{[e^{-\sqrt{A_1/A_0}L} - e^{\sqrt{A_1/A_0}L}]}e^{-\sqrt{A_1/A_0}Z}\end{aligned} \tag{54}$$

where

$$C_1 = \frac{1}{I_0(\sqrt{B}r_1)}\Big[\frac{1}{B}\frac{dP_0}{dZ} - C_2K_0(\sqrt{B}r_1)\Big] \tag{55}$$

$$C_2 = \frac{1}{B}\frac{dP_0}{dZ}\frac{I_0(\sqrt{B}r_1) - I_0(\sqrt{B}r_2)}{K_0(\sqrt{B}r_2)I_0(\sqrt{B}r_1) - I_0(\sqrt{B}r_2)K_0(\sqrt{B}r_1)} \tag{56}$$

$$C_3 = r_2M_e(P_0 - P_e) + \frac{r_2}{\sqrt{B}}\frac{\partial C_1}{\partial Z}I_1(\sqrt{B}r_2) - \frac{r_2}{\sqrt{B}}\frac{\partial C_2}{\partial Z}K_1(\sqrt{B}r_2) - \frac{r_2^2}{2B}\frac{d^2P_0}{dZ^2} \tag{57}$$

$$C_4 = P_a + \frac{A_2}{A_1} - \frac{(P_e + A_2/A_1 - [P_a + A_2/A_1]e^{\sqrt{A_1/A_0}L})}{[e^{-\sqrt{A_1/A_0}L} - e^{\sqrt{A_1/A_0}L}]} \tag{58}$$

$$C_5 = \frac{P_e + A_2/A_1 - [P_a + A_2/A_1]e^{\sqrt{A_1/A_0}L}}{e^{-\sqrt{A_1/A_0}L} - e^{\sqrt{A_1/A_0}L}} \tag{59}$$

2.3. Physiological parameters

Physiological Parameters

The real-life physiological parameters related to CSF flow in the glymphatic system for humans have been discussed in the literature. Xie et al. [48] presented an approximation for the value of intracranial pressure to be about $P_e \approx 2000$ N/m^{-2}. This is in line with the results of Sudres [49], who indicated that the ranges of intracranial pressure are $1300 \leq P_e \leq 2000$ N/m^{-2} and the ranges of inlet pressure P_a at entrance of PVS are $5 \times 10^{-7} \leq P_a \leq 5 \times 10^2$ N/m^{-2}. In this study, P_b is assumed with a very small value $P_b \approx 0$ compared with the inlet pressure P_a. Wang and Olbricht [50] presented that the measured values for the inner and outer radii of PVS layer are $r_1 \approx 10^{-5}$ m for the peristaltic wave and $r_2 \approx 1.1 \times 10^{-5}$ m for the neural tissue. Recent studies [51–55] reported the different values of the relevant physiological parameters as follows: the PVS

film thickness, $b \approx 10^{-6}$ m; the amplitude of the peristaltic wave, $\bar{h} \in [1.25, 5] \times 10^{-7}$ m; the speed of the peristaltic wave, $c \approx 1$ m/s (which cause a peristaltic wavelength of $\lambda \approx 0.2$ m); the dynamic viscosity, $\mu = 9 \times 10^{-4}$ Pa·s; and the fluid density compared to the one of water, $\rho \approx \rho_{\text{water}} = 10^3$ kg/m^3. Furthermore, Baumbach et al. [56] reported the wall thickness t_a of the arterial vessel to be 10 to 100 times smaller than r_1; i.e., $10^{-6} \leq t_a \leq 10^{-5}$ m. Additionally, the arterial vessel wall elastic modulus E_a has a range of $10^5 \leq E_a \leq 10^6$ N/m^{-2}. Finally, the neural tissue elasticity and the porosity factors were $E_g \approx 0.01$ Pa and $k_g \approx 10^{-11}$ m·Pa^{-1}s^{-1}. Based on these factors, the ranges of the nondimensional groups of interest for the present study are listed in Table 1. Notably, the lubrication theory is a strong approximation for the thin film cerebrospinal fluid flow for this study. Thus, this results in assumptions of long wavelength and low Reynolds number and small amplitude ratio [$\varepsilon \ll 1$ and $Re \ll 1$]. Thus, higher orders of ε and inertial effects due to Re are negligible.

The low Reynolds number indicated the high viscosity dominance created by viscous damping and the low inertial effect. The small CSF velocities vary between 10^{-5} and 10^{-6} m/s. Then, the estimated range for R_e was $[5 \times 10^{-12} : 2 \times 10^{-4}]$. The long wavelength approach was involved due to the short length scale for PVS width l. Then, the range for long wavelength λ was estimated as $[0.2 : 0.6]$, while the PVS length ($L = l/\lambda$) was $[2 : 20]$. This analysis concentrates on conditions where the Reynolds number is low, and inertial effects are negligible.

Table 1: Range of parameters.

Parameter	Characterization	Assessed range
Re	Reynolds number ($\varepsilon\rho\omega b^2/\mu$)	$[5 \times 10^{-12} : 2 \times 10^{-4}]$
ε	Film thickness of PVS (b/λ)	$[10^{-6} : 3.75 \times 10^{-2}]$
R_1	The PVS layer lumen radius (r_1/b)	$[0.7 : 10^3]$
$\bar{H}$	The peristalsis amplitude ($\bar{h}/b$)	$[8 \times 10^{-4} : 0.5]$
L	PVS length (l/λ)	$[2 : 20]$
M_e	Neural tissue porosity ($k_g\mu/b\varepsilon^2$)	$[10^{-2} : 10]$
E_e	Neural tissue stiffness ($E_g\varepsilon^2/\mu\omega(R_1+1)$)	$[2 \times 10^{-10} : 0.2]$

3. Results and Discussion

In this part, the study is focused on examining the movement of CSF across the neural tissue's neuroglial layer using a tribological framework formulated from first principles. The findings reveal that the phase difference between the arterial peristaltic wave and the neuroglial layer deformation is essential for breaking flow symmetry and establishing a steady streaming. This section depicts graphical illustrations for the behavior of the CSF flow, including the stream-direction velocity distribution $W_o(r, z)$, permeation velocity $U_e(r, z)$, pressure distribution $P_o(z)$, pressure gradient distribution $\frac{dP_o}{dZ}$, and the neural tissue deformation at the neuroglial elastic layer $D_o(r, z)$. The plots shown in Figures 3–19 are analyzed under the influence of key parameters including Hartmann Number (B),

neural tissue deformation (D_o) corresponding to the wall at R_2, neural tissue porosity (M_e), neural tissue stiffness (E_e), and pressure in the neural tissue (P_e). Figures 3–5 present the stream-direction velocity profiles of CSF along the radial direction under the influences of $\{B, M_e, P_e\}$. Figure 3 shows that the augmentation in Hartmann number exerts resistive action on the CSF flow by lowering the stream-direction velocity and reducing the CSF flow rate for the same cross-sectional area. The same effect is evident in Figure 4, where higher neural tissue porosity permits greater leakage of CSF at the neural tissue and decreases stream-direction velocity in the presence of a magnetostatic field. Figure 5 displays that the elevated neural tissue pressure (P_e) compresses the neuroglial wall toward the arterial vessel, reducing thin film thickness and restricting the flow path, and consequently lowering CSF flow velocity. The data for Figures 3–5 are summarized in Table 2.

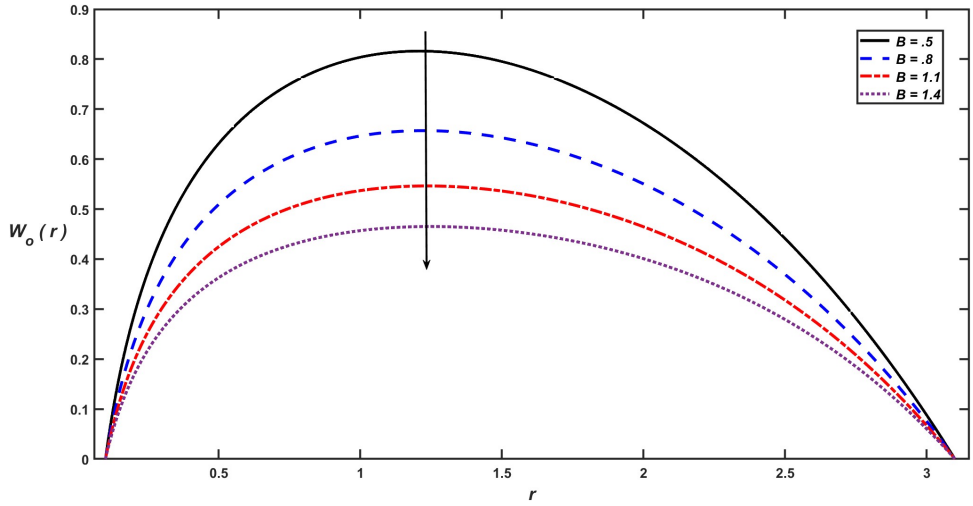

Figure 3: Effect of the magnetostatic flux intensity on the CSF stream-direction velocity.

Figures 6–8 illustrate the distribution of permeation velocity near the permeable neuroglial layer, which indicates the leakage velocity of CSF in the radial direction under the influence of the magnetostatic field, neural tissue deformation at the wall, and neural tissue porosity. Figure 6 demonstrates that the increase in the magnetostatic field causes restriction to the permeation velocity as the permeable area reduces and leakage decreases. Conversely, Figure 7 depicts that the increase in M_e is boosting the leakage of CSF at the neural tissue, consequently increasing the permeation velocity. The same effect is observed in Figure 8, where the increase in elastic neural tissue deformation enlarges the porous area of the permeable neuroglial layer and enhances the permeation velocity. The data for Figures 6–8 are summarized in Table 3.

Figures 9–13 illustrate the distribution of deformation in neuroglial permeable neural tissue under the external effects of a transverse magnetostatic field, pressure in the neural tissue, the elastic features of the brain represented by the stiffness of the neural tissue, and the neural tissue porosity. Moreover, they demonstrate that the increase in both the magnetostatic field B and pressure in the neural tissue P_e influence the elastic features

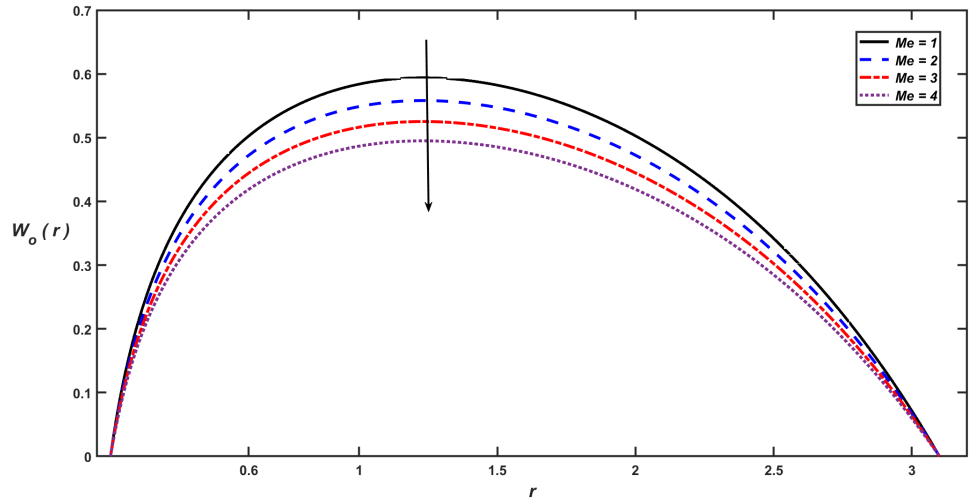

Figure 4: Effect of the neural tissue porosity on the CSF stream-direction velocity.

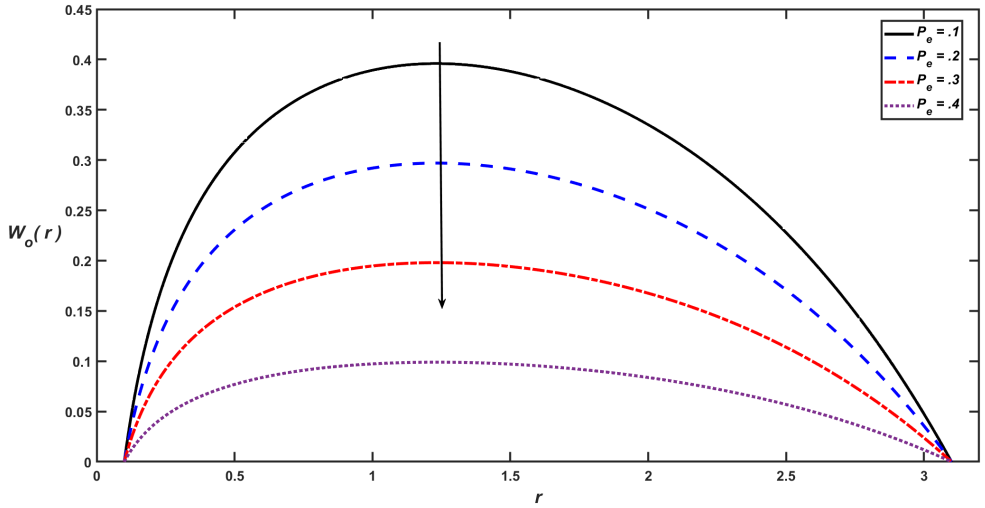

Figure 5: Effect of the pressure of neural tissue on the CSF stream-direction velocity.

of neural tissue deformability by reduction, see Figures 9–12. The same effect is noted in Figures 10–11 as evidenced by the inversely proportional relationship between the brain deformation and both neural tissue stiffness and porosity. Figure 13 indicates that the increase in the lumen radius of PVS layer R_1 is slightly increasing the deformation of the neuroglial permeable neural tissue. The data for Figures 9–13 are summarized in Table 4.

Figures 14–16 highlight the pressure distribution along the stream-direction direction. Figure 14 reports that the augmentation of the magnetostatic field reduces the pressure distribution across the CSF flow, as evidenced by the reduction in total energy relevant to the effect of magnetostatic strength on the stream-direction velocity. Quantitative analysis of the results reveals that the non-dimensional pressure drop increases noticeably with the augmentation in the Hartmann number. The stronger magnetic fields enhance the Lorentz

Table 2: Representative values of physical parameters related to Figures 3–5

Figures	R_1	Z	B	M_e	P_e	D_o	P_a	L
Figure 3	0.1	0.5	0.5 0.8 1.1 1.4	2	0.2	1	0.5	0.5
Figure 4	0.1	0.5	0.8	1 2 3 4	0.2	1	0.5	0.5
Figure 5	0.1	0.5	0.8	2	0.1 0.2 0.3 0.4	1	0.5	0.5

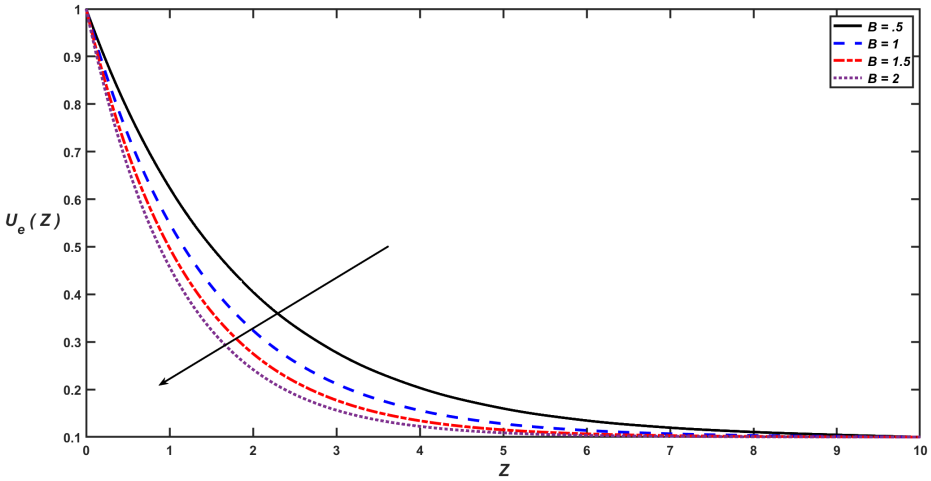

Figure 6: Influence of the magnetostatic flux intensity on the CSF permeation velocity.

force and increase the effective resistance to CSF motion. The pressure distribution shows that a rise in B from 0.5 to 2 results in approximately a 15–25% increase in the pressure drop across one wavelength of the peristaltic channel. In contrast, Figure 15 shows that the increase in neural tissue porosity results in boosting the leakage of CSF at the neural tissue, consequently increasing the permeation velocity. The same effect is observed in Figure 16, where the increase in elastic neural tissue deformation enlarges the porous area of the permeable neuroglial layer and enhances the permeation velocity. The data for Figures 14–16 are presented in Table 5.

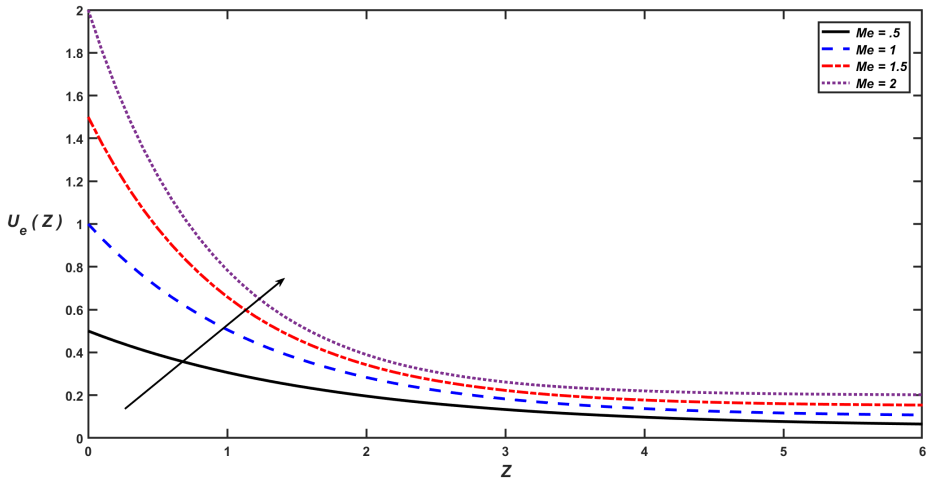

Figure 7: Influence of the porosity of neural tissue on the CSF permeation velocity .

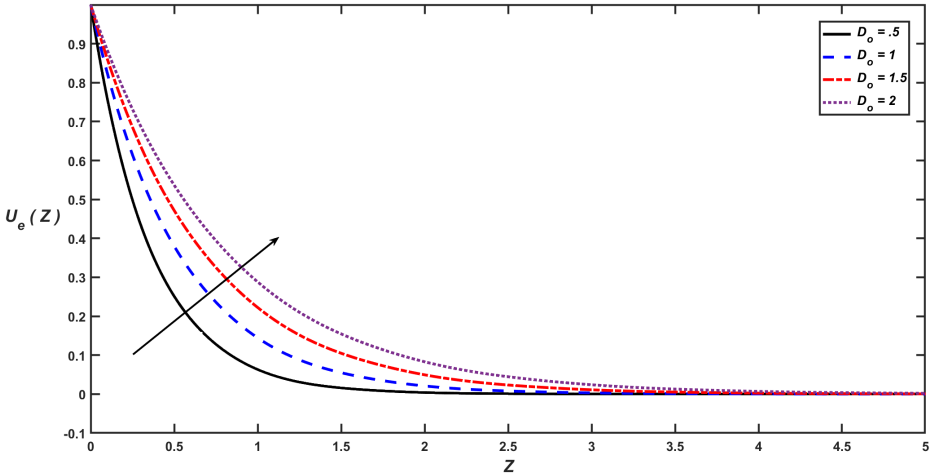

Figure 8: Influence of the deformation of the neural tissue on the CSF permeation velocity.

Table 5: Representative values of physical parameters related to Figures 14–16.

Figures	R_1	B	M_e	D_o	P_e	P_a	L
Figure 14	0.1	0.5 1 1.5 2	1	1.5	0.01	0.5	10
Figure 15	0.1	1	0.5 1 1.5 2	1.5	0.01	0.5	10
Figure 16	0.1	1	1	0.5 1 1.5 2	0.01	0.5	10

Table 3: Representative values of physical parameters related to Figures 6–8.

Figures	R_1	E_e	B	M_e	D_o	P_e	P_a	L
Figure 6	0.1	0.2	0.5 1 1.5 2	1	1.5	0.01	1	10
Figure 7	0.1	0.2	1	0.5 1 1.5 2	1.5	0.01	1	0.5
Figure 8	0.1	0.2	1	1	0.5 1 1.5 2	0.01	1	0.5

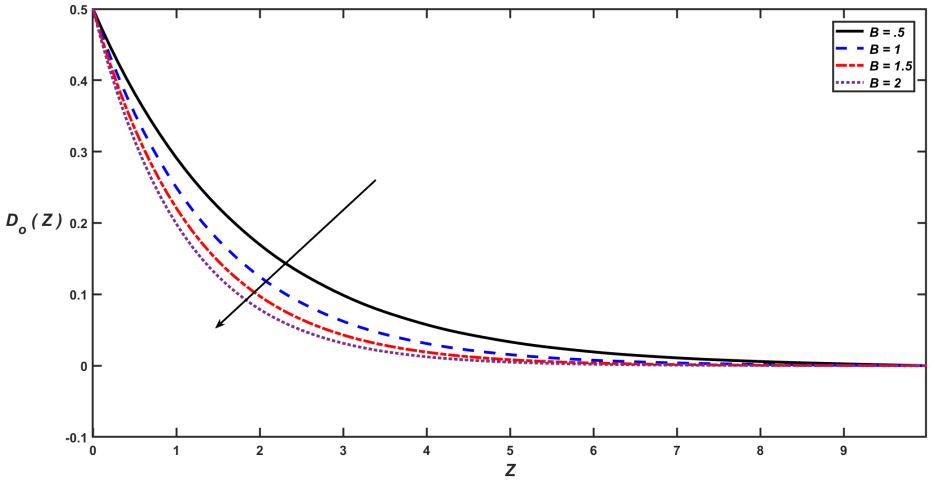

Figure 9: Influence of the magnetostatic flux intensity on the deformation of neural tissue.

Figures 17–19 demonstrate the influences of magnetostatic field B, deformation of neural tissue D_o, and neuroglial layer porosity of neural tissue. Figure 17 shows that the pressure gradient increases with the length of PVS. For short length of PVS $[0 \leq z \leq 1.28]$, the increase in magnetostatic field strength reduces the pressure gradient, and it becomes a more negative pressure gradient, which assists the flow velocity and indicates normal streaming. In contrast, for long length of $[z > 1.28]$, the increase in magnetostatic field boosts the chances of reversal when a large positive pressure gradient appears, as it resists the flow and reduces the kinetic energy of the CSF streaming. Notably, the positive pressure gradients are not achieved under the present condition, and backflow does not occur. The same effect of preamble neuroglial layer on the pressure gradient is seen in Figure 19, with critical conditions for PVS length, where for short length of PVS $[0 \leq z \leq 1.28]$, an inversely proportional relationship between M_e and dP_o/dZ occurs and the pressure gradient becomes more negative, unlike the conditions for long length of

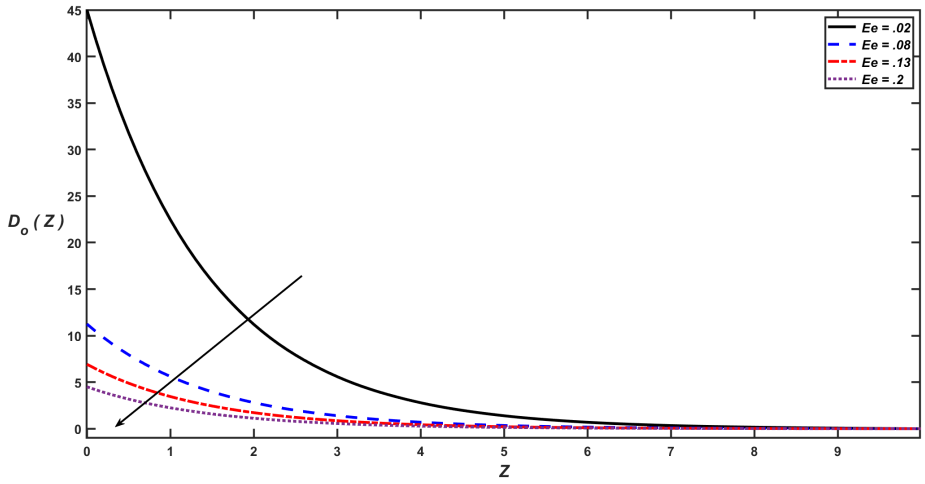

Figure 10: Influence of the stiffness of neural tissue on the deformation of neural tissue.

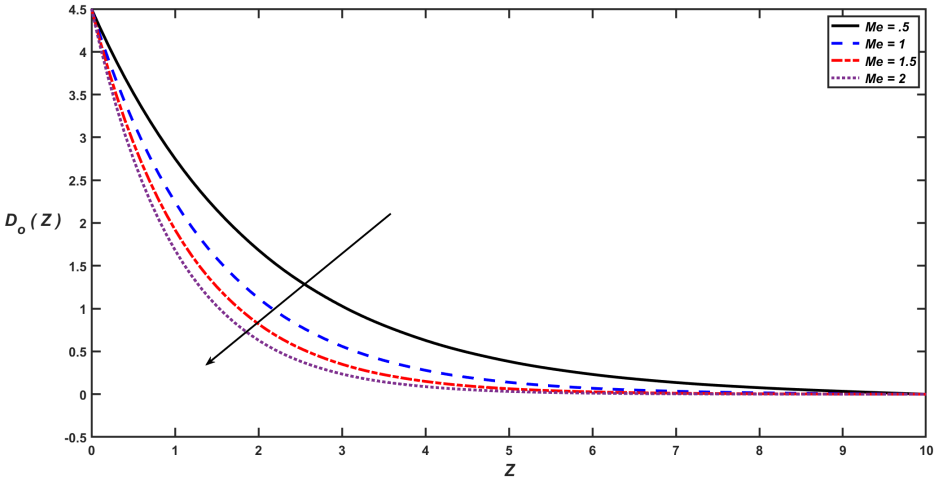

Figure 11: Influence of the porosity parameter on the deformation of neural tissue.

$[z > 1.28]$. The effect of the brain tissue deformation on the pressure gradient has opposite manner compared to magnetic field and space porosity influences, as shown in Figure 18. The data for Figures 17–19 are presented in Table 6.

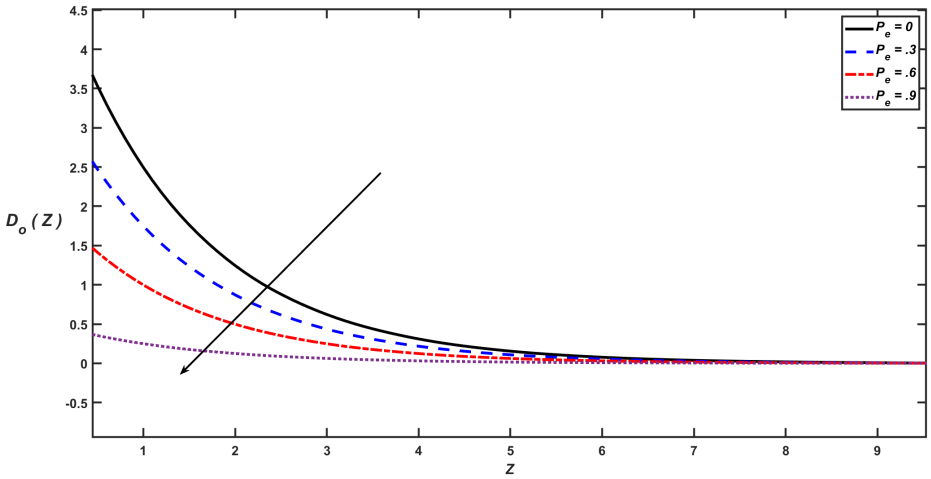

Figure 12: Influence of the pressure in the neural tissue on the deformation of neural tissue.

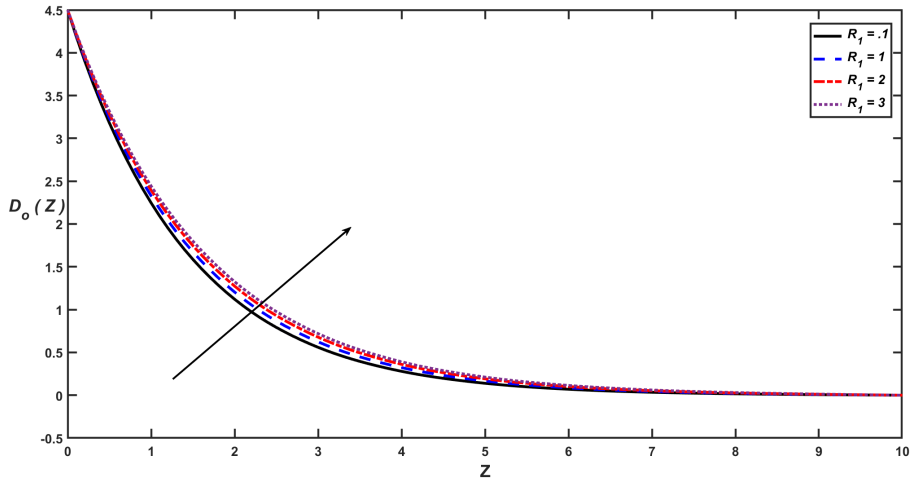

Figure 13: Influence of the lumen radius of the PVS layer on the deformation of neural tissue.

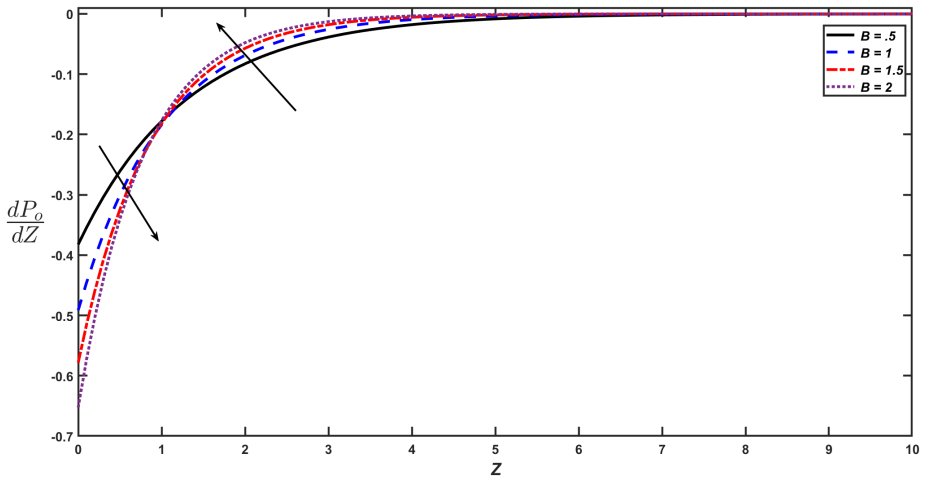

Figure 17: Effect of the magnetostatic flux intensity on the CSF pressure gradient distribution.

Table 4: Representative values of physical parameters related to Figures 9–13.

Figures	L	P_a	B	E_e	M_e	P_e	R_1
Figure 9	10	1	0.5 1 1.5 2	0.2	1	0.1	0.1
Figure 10	10	1	1	0.02 0.08 0.13 0.2	1	0.1	0.1
Figure 11	10	1	1	0.2	0.5 1 1.5 2	0.1	0.1
Figure 12	10	1	1	0.2	1	0 0.3 0.6 0.9	0.1
Figure 13	10	1	1	0.2	1	0.1	0.1 1 2 3

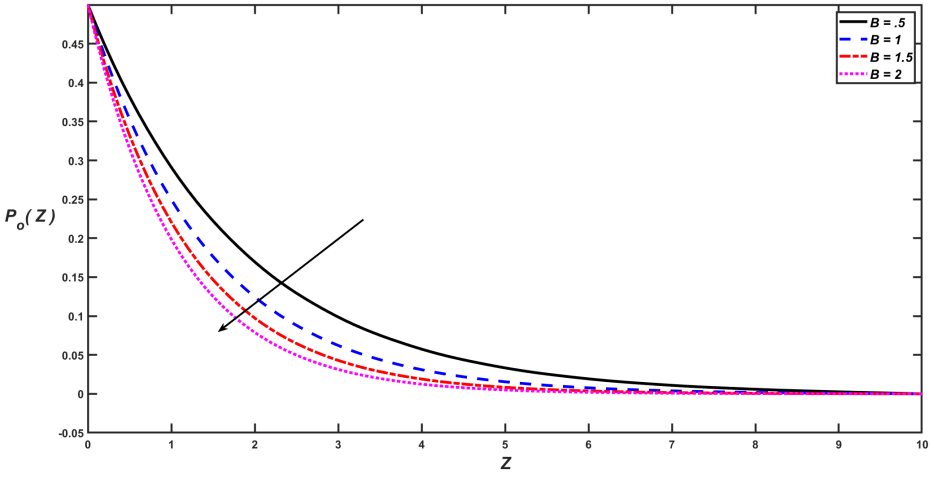

Figure 14: Effect of the magnetostatic flux intensity on the CSF pressure distribution.

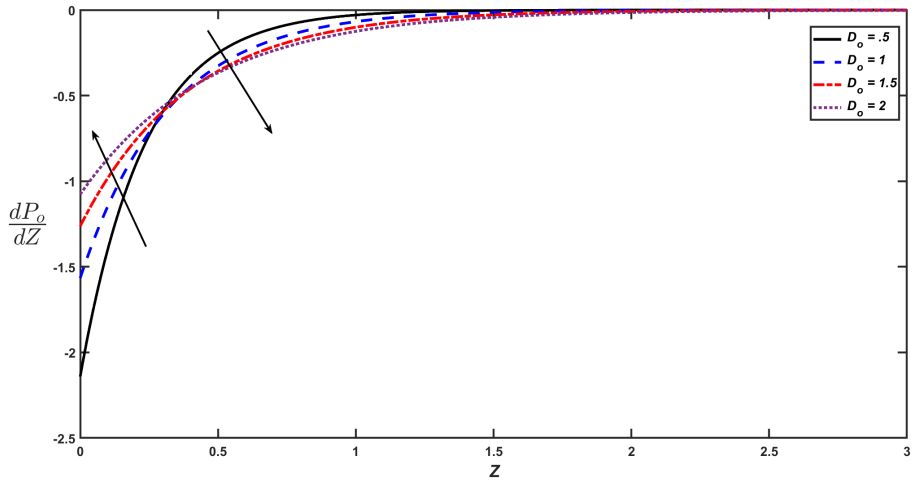

Figure 18: Effect of the deformation of neural tissue on the CSF pressure gradient distribution.

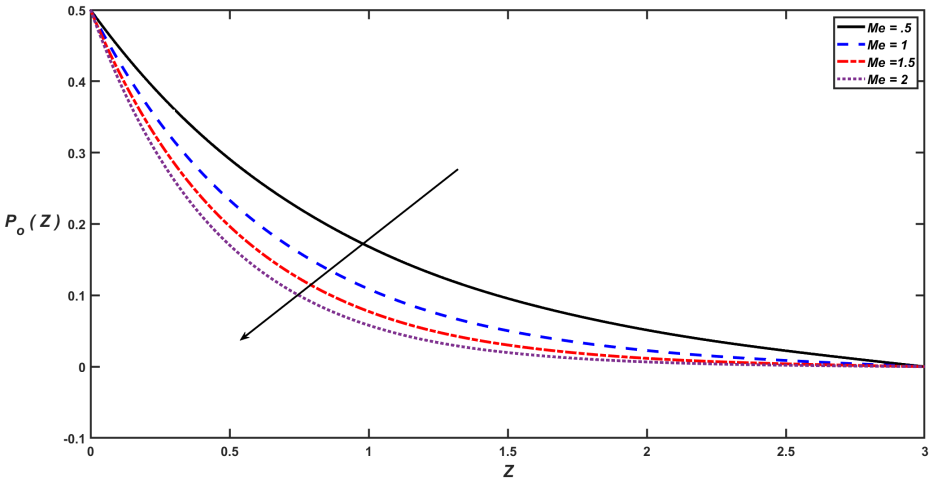

Figure 15: Effect of the porosity of neural tissue on the CSF pressure distribution.

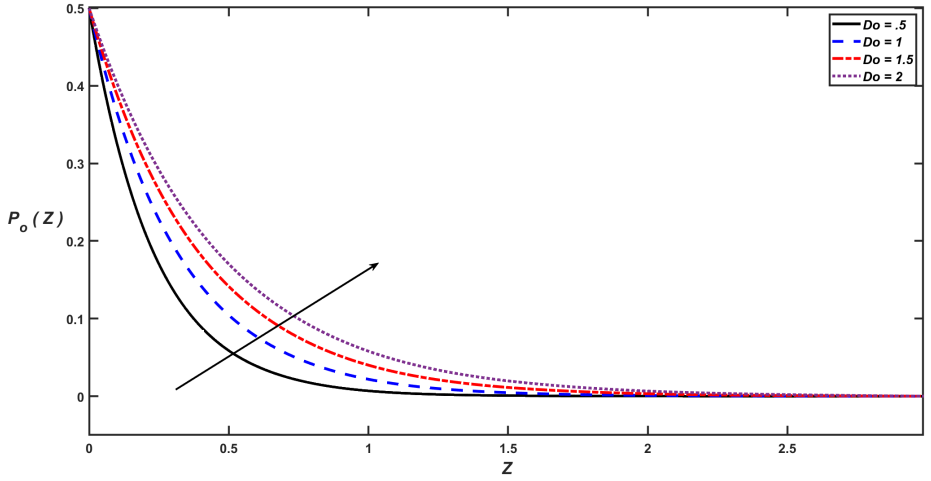

Figure 16: Effect of the deformation of neural tissue on the CSF pressure distribution.

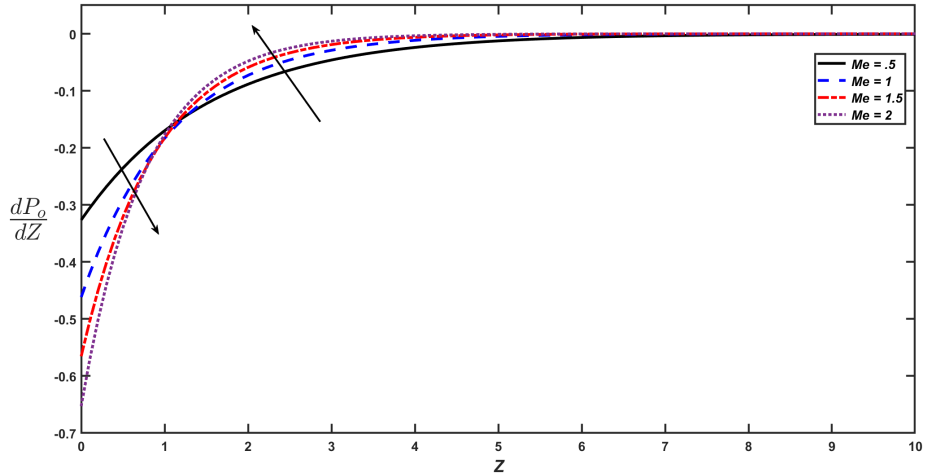

Figure 19: Effect of the porosity of neural tissue on the CSF pressure gradient distribution.

Table 6: Representative values of physical parameters related to Figures 17–19.

Figures	L	P_a	B	D_o	M_e	R_1	P_e
Figure 17	5	0.5	0.5	2	1	0.1	0.01
			1				
			1.5				
			2				
Figure 18	5	0.5	1	0.5	1	0.1	0.01
				1			
				1.5			
				2			
Figure 19	5	0.5	1	2	0.5	0.1	0.01
					1		
					1.5		
					2		

4. Conclusion

This section presents a conclusion based on a comprehensive graphical analysis of the results, emphasizing the critical factors that affect the performance of various physiological and physical parameters on the peristaltic flow of cerebrospinal fluid through the glymphatic system model, including magnetostatic field parameter (B), neural tissue deformation parameter corresponding to wall (D_o), porosity parameter of the neural tissue (M_e), stiffness parameter of the neural tissue (E_e), and pressure in the neural tissue (P_e). This analysis provides important insights into how magnetic fields and porous neuroglial properties modulate CSF transport within the glymphatic system. The results indicate that increasing the magnetostatic field enhances the Lorentz force with resistive action and reduces CSF axial velocity $W_o(r)$, the permeation velocity $U_e(z)$, the deformation of the neural tissue (D_o), and the pressure distribution along the stream-direction $P_o(z)$. For most people, it is preferable to be far away from sources of magnetostatic fields, such as mobile phones, especially during sleep. The porosity of neural tissue (M_e) has a sensitive effect on the CSF properties, as the increase of M_e causes a reduction in the CSF axial velocity, the deformation of the neural tissue, and the pressure distribution along the stream-direction $P_o(z)$, while increasing the permeation velocity $U_e(z)$. The pressure in the neural tissue (P_e) has an adverse effect on both the CSF flow stream-direction velocity $W_o(r)$ and the deformation of neural tissue (D_o). The stiffness parameter of the neural tissue (E_e) has a direct effect on the pressure distribution along the stream-direction $P_o(z)$; on the other hand, it has an adverse effect on the deformation of neural tissue. These outcomes recommend that the utility of the magnetic field provides a potential effect on glymphatic clearance rates and, consequently, the removal of metabolic waste from the brain. From a clinical perspective, this can develop implications for magnetically guided therapeutic techniques or drug delivery systems targeting neurological disorders such as Alzheimer's disease, Parkinson's disease, and traumatic brain injury. Furthermore, the

insights gained from this model can serve as a foundation for future studies aimed at optimizing external magnetic field parameters to enhance and regulate CSF dynamics in both diagnostic and therapeutic contexts.

Conflict of interests

No conflict of interests.

Funding

The authors extend their appreciation to Prince Sattam bin Abdulaziz University for funding this research work through the project number (PSAU/2025/01/34000).

Acknowledgements

The authors extend their appreciation to Prince Sattam bin Abdulaziz University for funding this research work through the project number (PSAU/2025/01/34000).

References

[1] Y. Gao, K. Liu, and J. Zhu. Glymphatic system: an emerging therapeutic approach for neurological disorders. *Frontiers in Molecular Neuroscience*, 16:1138769, 2023.

[2] L. M. Hablitz and M. Nedergaard. The glymphatic system. *Current Biology*, 31(20):R1371–R1375, 2021.

[3] L.-H. Wang, Z.-L. Wang, W.-Y. Chen, M.-J. Chen, and G.-Y. Xu. The glymphatic system: concept, function and research progresses. *Sheng Li Xue Bao [Acta Physiologica Sinica]*, 70(1):52–60, 2018.

[4] K. Astara et al. A novel conceptual framework for the functionality of the glymphatic system. *Journal of Neurophysiology*, 129(5):1228–1236, 2023.

[5] E. F. Camargos and O. T. Nóbrega. Revisiting old drugs owing to the glymphatic system: A step toward unlocking the role of hypnotics in brain health. *The Journal of Clinical Pharmacology*, 63(6):745–746, 2023.

[6] L. N. Telano and S. Baker. *Physiology, cerebral spinal fluid*. StatPearls Publishing, Treasure Island (FL), 2018.

[7] H. Soytürk, M. Yılmaz, C. Önal, E. Suveren, and Ü. Kılıç. Circulation of cerebrospinal fluid (csf). *Cerebrospinal Fluid*, page 21, 2021.

[8] R. M. Abumandour, I. M. Eldesoky, and E. T. Abdelwahab. On the performance of peristaltic pumping for the mhd slip flow under the variation of elastic walls features. *ERJ. Engineering Research Journal*, 43(3):231–244, 2020.

[9] R. M. Abumandour, I. M. Eldesoky, E. T. Abdelwahab, and M. M. Ahmed. Conjugate dissipative radiative heating with thermal slipping and the entropy production on the thrust of mhd gold blood nanofluid with curvature effects. *ZAMM-Journal of Applied*

Mathematics and Mechanics/Zeitschrift für Angewandte Mathematik und Mechanik, 104(2):e202300260, 2024.

[10] L. K. Antanovskii and H. Ramkissoon. Long-wave peristaltic transport of a compressible viscous fluid in a finite pipe subject to a time-dependent pressure drop. *Fluid Dynamics Research*, 19(2):115, 1997.

[11] C. D. Dimitropoulos, B. J. Edwards, K.-S. Chae, and A. N. Beris. Efficient pseudospectral flow simulations in moderately complex geometries. *Journal of Computational Physics*, 144(2):517–549, 1998.

[12] I. Eldesoky, R. Abumandour, M. Kamel, and E. Abdelwahab. The combined influences of heat transfer, compliant wall properties and slip conditions on the peristaltic flow through tube. *SN Applied Sciences*, 1:1–16, 2019.

[13] I. Eldesoky, R. Abumandour, M. Kamel, and E. Abdelwahab. The combined effects of wall properties and space porosity on mhd two-phase peristaltic slip transport through planar channels. *International Journal of Applied and Computational Mathematics*, 7:1–37, 2021.

[14] I. M. Eldesoky, R. M. Abumandour, and E. T. Abdelwahab. Analysis for various effects of relaxation time and wall properties on compressible maxwellian peristaltic slip flow. *Zeitschrift für Naturforschung A*, 74(4):317–331, 2019.

[15] O. Eytan, A. J. Jaffa, and D. Elad. Peristaltic flow in a tapered channel: application to embryo transport within the uterine cavity. *Medical Engineering & Physics*, 23(7):475–484, 2001.

[16] T. Hayat, A. Tanveer, H. Yasmin, and A. Alsaedi. Effects of convective conditions and chemical reaction on peristaltic flow of eyring-powell fluid. *Applied Bionics and Biomechanics*, 11(4):221–233, 2014.

[17] R. Lakshmi and A. Kavitha. Peristaltic motion of a casson nanofluid in a vertical layer with suction and injection. *International Journal of Modern Physics B*, 38(17):2450212, 2024.

[18] A. A. Shaaban and M. Y. Abou-Zeid. Effects of heat and mass transfer on mhd peristaltic flow of a non-newtonian fluid through a porous medium between two coaxial cylinders. *Mathematical Problems in Engineering*, 2013(1):819683, 2013.

[19] V. Srivastava and M. Saxena. A two-fluid model of non-newtonian blood flow induced by peristaltic waves. *Rheologica Acta*, 34:406–414, 1995.

[20] E. Tharwat, M. Magdy, I. M. Eldesoky, and R. M. Abumandour. Heating and slipping effects on gold-blood flow of nanofluid consequent to peristaltic waves with various shape factors in a vertical tube: Cancer treatment. *ERJ. Engineering Research Journal*, 46(4):555–576, 2023.

[21] M. A. Ghafor. *Peristaltic motion of a magnetohydrodynamics Oldroyd-B fluid in planar channel with heat transfer*. PhD thesis, Universiti Teknologi Malaysia, 2014.

[22] F. Romanò, V. Suresh, P. A. Galie, and J. B. Grotberg. Peristaltic flow in the glymphatic system. *Scientific Reports*, 10(1):21065, 2020.

[23] M. K. Sharp. Pulsatile paraarterial flow by peristalsis, pressure and directional resistance. 2022.

[24] K. Yazdanpanh-Ardakani and H. Niroomand-Oscuii. New approach in modeling peri-

staltic transport of non-newtonian fluid. *Journal of Mechanics in Medicine and Biology*, 13(04):1350052, 2013.

[25] L. M. Hablitz and M. Nedergaard. The glymphatic system: a novel component of fundamental neurobiology. *Journal of Neuroscience*, 41(37):7698–7711, 2021.

[26] O. Balédent and I. Idy-Peretti. Cerebrospinal fluid dynamics and relation with blood flow: a magnetostatic resonance study with semiautomated cerebrospinal fluid segmentation. *Investigative Radiology*, 36(7):368–377, 2001.

[27] S. A. Smith. *Development of magnetostatic resonance saturation techniques to detect and quantify macromolecular pathologies afflicting the brain and spinal cord*. PhD thesis, The Johns Hopkins University, 2006.

[28] R. I. Mehta et al. Blood-brain barrier opening with mri-guided focused ultrasound elicits meningeal venous porosity in humans with early alzheimer disease. *Radiology*, 298(3):654–662, 2021.

[29] A. Lonappan, V. Thomas, G. Bindu, C. Rajasekaran, and K. Mathew. Analysis of human cerebro spinal fluid at the ism band of frequencies. *Journal of Electromagnetostatic Waves and Applications*, 20(6):773–779, 2006.

[30] E. A. M. Ali. Effect of magnetostatic field from mobile phone on central nervous system. *Journal of Advances in Physics*, 8(3), 2018.

[31] A. W. Preece. *Cognitive Effects of Electromagnetostatic Fields in Humans*, pages 133–165. 2009.

[32] D. Schley, R. Carare-Nnadi, C. Please, V. Perry, and R. Weller. Mechanisms to explain the reverse pvs transport of solutes out of the brain. *Journal of Theoretical Biology*, 238(4):962–974, 2006.

[33] P. Hadaczek et al. The "pvs pump" driven by arterial pulsation is a powerful mechanism for the distribution of therapeutic molecules within the brain. *Molecular Therapy*, 14(1):69–78, 2006.

[34] J. J. Iliff et al. Cerebral arterial pulsation drives paravascular csf–interstitial fluid exchange in the murine brain. *Journal of Neuroscience*, 33(46):18190–18199, 2013.

[35] H. Mestre et al. Flow of cerebrospinal fluid is driven by arterial pulsations and is reduced in hypertension. *Nature Communications*, 9(1):4878, 2018.

[36] S. I. Abdelsalam, E. T. Abdelwahab, I. Eldesoky, R. M. Abumandour, and M. Ahmed. Benchmarking the composite performance of distinct shapes of ferrometallic gold nanoshells: photothermal cancer therapy. *Acta Mechanica Sinica*, 41(6):724077, 2025.

[37] S. I. Abdelsalam, N. Alsedais, and A. M. Aly. Revolutionizing bioconvection: Artificial intelligence-powered nano-encapsulation with oxytactic microorganisms. *Engineering Applications of Artificial Intelligence*, 137:109128, 2024.

[38] S. I. Abdelsalam and M. Bhatti. Synergistic progression of nanoparticle dynamics in stenosed arteries. *Qualitative Theory of Dynamical Systems*, 24(1):6, 2025.

[39] S. I. Abdelsalam, M. A. Dagher, Y. Abd Elmaboud, and A. Abdellateef. Towards understanding thermal management in unsteady boundary layer flow with ac/dc electric fields. *Propulsion and Power Research*, 14(1):64–75, 2025.

[40] S. I. Abdelsalam, A. Magesh, and P. Tamizharasi. Optimizing fluid dynamics: An in-depth study for nano-biomedical applications with a heat source. *Journal of Thermal*

Analysis and Calorimetry, 150(4):2781–2793, 2025.

[41] N. Alsedais, M. A. Mansour, A. M. Aly, and S. I. Abdelsalam. Artificial neural network validation of mhd natural bioconvection in a square enclosure: entropic analysis and optimization. *Acta Mechanica Sinica*, 41(9):724507, 2025.

[42] N. Elsedais, M. A. Mansour, A. M. Aly, and S. Abdelsalam. Artificial intelligence-driven fvm-ann model for entropy analysis of mhd natural bioconvection in nanofluid-filled porous cavities. 2024.

[43] M. El Kot, A. M. Alsharif, Y. Abd Elmaboud, and S. I. Abdelsalam. Harnessing electroosmotic hybrid nanofluid dynamics in curved arteries: insights into biomedical flow enhancement. *Frontiers in Nanotechnology*, 6:1520183, 2024.

[44] A. Saleem, S. Akhtar, F. M. Alharbi, S. Nadeem, M. Ghalambaz, and A. Issakhov. Physical aspects of peristaltic flow of hybrid nano fluid inside a curved tube having ciliated wall. *Results in Physics*, 19:103431, 2020.

[45] A. Saleem, S. Akhtar, S. Nadeem, F. M. Alharbi, M. Ghalambaz, and A. Issakhov. Mathematical computations for peristaltic flow of heated non-newtonian fluid inside a curved tube having ciliated wall. *Physica Scripta*, 95(10):105009, 2020.

[46] A. Saleem, A. Qaiser, S. Nadeem, M. Ghalambaz, and A. Issakhov. Physiological flow of non-newtonian fluid with variable density inside a ciliated symmetric channel having compliant wall. *Arabian Journal for Science and Engineering*, 46:801–812, 2021.

[47] Z. Abbas, M. Rafiq, A. Alshomrani, and M. Ullah. Analysis of entropy generation on peristaltic phenomena of mhd slip flow of viscous fluid in a diverging tube. *Case Studies in Thermal Engineering*, 23:100817, 2021.

[48] X. Xie et al. Noninvasive intracranial pressure estimation by orbital subarachnoid space measurement: the beijing intracranial and intraocular pressure (icop) study. *Critical Care*, 17(4):R162, 2013.

[49] P. Sudres. *Biomechanics between the cerebrospinal fluid and the spinal central nervous system: towards a modelling of fluid-structure interactions*. PhD thesis, Université Aix-Marseille, 2021.

[50] P. Wang and W. L. Olbricht. Fluid mechanics in the pvs space. *Journal of Theoretical Biology*, 274(1):52–57, 2011.

[51] L. E. Bilston, D. F. Fletcher, A. R. Brodbelt, and M. A. Stoodley. Arterial pulsation-driven cerebrospinal fluid flow in the pvs space: a computational model. *Computer Methods in Biomechanics & Biomedical Engineering*, 6(4):235–241, 2003.

[52] S. Gladdish, D. Manawadu, W. Banya, J. Cameron, C. J. Bulpitt, and C. Rajkumar. Repeatability of non-invasive measurement of intracerebral pulse wave velocity using transcranial doppler. *Clinical Science*, 108(5):433–439, 2005.

[53] A. Hoeks, P. Brands, J. Willigers, and R. Reneman. Non-invasive measurement of mechanical properties of arteries in health and disease. *Proceedings of the Institution of Mechanical Engineers, Part H: Journal of Engineering in Medicine*, 213(3):195–202, 1999.

[54] T. Ichimura, P. Fraser, and H. F. Cserr. Distribution of extracellular tracers in pvs spaces of the rat brain. *Brain Research*, 545(1-2):103–113, 1991.

[55] E. N. Lightfoot. *Transport phenomena and living systems: biomedical aspects of momentum and mass transport*. 1974.

[56] G. L. Baumbach, D. D. Heistad, and J. Siems. Effect of sympathetic nerves on composition and distensibility of cerebral arterioles in rats. *The Journal of Physiology*, 416(1):123–140, 1989.